Environmental Science Nano

ROYAL SOCIETY OF CHEMISTRY

PAPER

View Article Online
View Journal

Published on 28 August 2020. Downloaded by Indian Institute of Technology Kanpur on 11/11/2020 10:27:41 PM.

Check for updates

Cite this: DOI: 10.1039/d0en00660b

Transition metal-doped MgO nanoparticles for nutrient recycling: an alternate Mg source for struvite synthesis from wastewater†

Manoj Silva, [a] Vadim Murzin, [bc] Lihua Zhang,[d] John Baltrus [e] and Jonas Baltrusaitis *[a]

Nutrient nitrogen (N) and phosphorus (P) recovery from wastewater is an important challenge for enhanced environmental sustainability. Herein we report the synthesis and properties of mesoporous MgO nanoparticles doped with copper (Cu), iron (Fe), and zinc (Zn) as an alternative low-solubility high-abundance magnesium (Mg) source for crystalline struvite precipitation from nutrient-laden wastewater. Undoped MgO was shown to have the fastest phosphate (PO_4^{3-}) adsorption kinetics with a k_2 value of 0.9 g g^{-1} min^{-1} at room temperature. The corresponding rate constant decreased for Cu–MgO (0.175 g g^{-1} min^{-1}), Zn–MgO (0.145 g g^{-1} min^{-1}), and Fe–MgO (0.02 g g^{-1} min^{-1}). Undoped MgO resulted in the highest PO_4^{3-} removal at 94%, while Cu–MgO, Fe–MgO, and Zn–MgO resulted in 90%, 66% and 66%, respectively, under equivalent reaction conditions. All dopants resulted in the production of struvite as the main product with the incorporation of the transition metals into the struvite crystal lattice. X-ray absorption spectroscopy (XAS) showed that the majority of the Cu, Fe, and Zn were primarily in the +2, +3, and +2 oxidation states, respectively. XAS also showed that the Cu atoms exist in elongated octahedral coordination, while Fe was shown to be in octahedral coordination. Zn was shown to be in a complex disordered environment with octahedral sites coexisting with the majority of the tetrahedral sites. Finally, X-ray photoelectron spectroscopy data suggest a two-fold struvite surface enrichment with dopant metals, with Cu exhibiting an interesting new local binding structure. The dopant concentrations utilized were consistent with those found in natural Mg minerals, suggesting that (a) utilizing natural mineral periclase as the Mg source for struvite production can result in struvite formation, albeit at the expense of the reaction kinetics and overall yields, while also (b) supplying essential micronutrients, such as Zn and Cu, necessary for balanced nutrient uptake.

Received 30th June 2020,
Accepted 27th August 2020

DOI: 10.1039/d0en00660b

rsc.li/es-nano

Environmental significance

High concentrations of phosphorous and nitrogen nutrients in agricultural wastewater lead to eutrophication of water sources, which adversely affects aquatic ecosystems and results in greenhouse gas emissions. To sustainably capture and recycle these nutrients to agricultural systems, we studied the use of nanostructured MgO as analogs for natural mineral-based Mg sources to produce struvite from wastewater. Undoped and Cu-, Fe-, and Zn-doped nanostructured MgO samples were produced *via* a facile sol–gel synthesis method. The porosity and high surface area achieved without the use of any support material allowed for enhanced transport of phosphate ions, leading to fast struvite formation kinetics for undoped MgO. The addition of transition metals inhibited phosphate adsorption compared to the undoped MgO.

Introduction

Modern mineral fertilizers have revolutionized agriculture by dramatically increasing productivity but have also exhibited detrimental effects on the global nutrient cycles in the environment.[1–3] Nitrogen (N) fertilizer production requires high energy input and results in net positive carbon dioxide emissions but up to 90% of the applied N can be lost *via* either runoff or greenhouse gas emissions.[2,4] Phosphorous (P) is a mined nutrient and is considered to be used

[a] *Department of Chemical and Biomolecular Engineering, Lehigh University, B336 Iacocca Hall, 111 Research Drive, Bethlehem, PA 18015, USA. E-mail: job314@lehigh.edu; Tel: +1 610 758 6836*
[b] *Deutsches Elektronen Synchrotron DESY, D-22607 Hamburg, Germany*
[c] *Bergische Universität Wuppertal, Gaußstraße 20, D-42119, Wuppertal, Germany*
[d] *Brookhaven National Laboratory, Center for Functional Nanomaterials, Upton, NY 11973, USA*
[e] *National Energy Technology Laboratory, U.S. Department of Energy, 626 Cochrans Mill Road, Pittsburgh, PA 15236, USA*

† Electronic supplementary information (ESI) available. See DOI: 10.1039/d0en00660b

Published on 28 August 2020. Downloaded by Indian Institute of Technology Kanpur on 11/11/2020 10:27:41 PM.

unsustainably.[5] Both N and P are lost from agricultural systems into the watershed, resulting in eutrophication that causes greenhouse gas emission, restriction to freshwater, and destruction of aquatic ecosystems.[6] Capturing nutrients from any wastewater and reusing them in agriculture can be viewed as an integral part of the circular economy. Nutrient-rich municipal and industrial wastewater can contain between 100 and 5000 ppm of total N and up to 1200 ppm of total P.[7] Struvite ($MgNH_4PO_4{\cdot}6H_2O$) crystallization allows for simultaneous removal of NH_4^+ and PO_4^{3-} from nutrient-laden wastewater by forming a solid fertilizer material. Struvite is a low-solubility mineral (pKsp = 13.36)[8] that exhibits slow nutrient release properties.[9] The scientific literature on struvite precipitation from wastewater chiefly focuses on the use of water-soluble magnesium precursor salts, such as magnesium chloride ($MgCl_2$).[9,10] However, $MgCl_2$ production from seawater or brine is energy-intensive and renders the struvite precipitation process less environmentally sustainable.[11,12] Therefore, the use of low-cost and more sustainable Mg sources is desired.

The use of earth-abundant low-solubility magnesium sources for struvite crystallization, such as periclase (MgO),[13–17] magnesite ($MgCO_3$),[18,19] brucite ($Mg(OH)_2$),[20] and dolomite ($CaMg(CO_3)_2$),[21–23] has been recently reported in the literature, resulting in up to 80% NH_4^+ removal. These minerals present an abundant and low-cost source of Mg for struvite precipitation.[13] Importantly, in contrast to using $MgCl_2$ where homogeneous nucleation results in struvite growth, a low-solubility magnesium mineral has to undergo a heterogeneous surface reaction leading to struvite crystallization. This results in unique reaction kinetics and growth mechanisms as well as the reactive intermediates so far explored to a limited extent.[21] A study using MgO supported on diatomite[14] investigated the effect of MgO dispersion over a high surface area substrate and reported faster kinetics than the microcrystalline MgO by virtue of the measured higher pseudo-second-order reaction constant.[13] However, the use of mesoporous MgO without the use of a support for struvite crystallization has not been widely reported in the literature. Another facet of the heterogeneous struvite crystallization problem is the effect of transition metals commonly present in wastewater. Cu, Fe and Zn are typically present in anthropogenic wastewater.[24,25] There are only a few studies on their effects on struvite formation kinetics as well as the complex structure of the resulting struvite.[25–27] For example, the effect of Cu and Zn present in solution on struvite formation using $MgCl_2$ has been reported as well as the adsorption of these metal ions on the formed struvite product.[25–29] Using extended X-ray absorption fine structure spectroscopy (EXAFS), Cu was shown to adsorb on the struvite surface in four-fold coordination while Zn was shown to exist in a mixed coordination environment with more tetrahedrally coordinated Zn centers.[26] However, the effect on the struvite formation kinetics of transition metals present in the heterogeneous MgO structure has not been studied previously.

The current study aims to synthesize nanostructured low-solubility MgO nanoparticles for struvite production to accelerate the underlying reaction kinetics. We report that mesoporous MgO can be fabricated as a nanostructured material with high surface area and porosity without requiring a support while also allowing fast intraparticle diffusion and faster surface reaction rates due to the increased number of adsorption sites. Furthermore, the effects of transition metals present in these model MgO nanoparticles on the kinetics, equilibrium concentrations and product characterization are presented. Natural Mg minerals contain up to 5% of transition metals such as Cu, Zn, and Fe, and thus, utilization of natural Mg minerals or transition metal-doped nanomaterials have significant environmental implications for the global nutrient cycles.[30–33] While previous reports have theoretically demonstrated that the adsorption properties of the MgO surface change with the addition of these metals,[34] the effects of these metals under struvite formation conditions have not been reported previously. Utilization of mesoporous MgO allows for the study of model systems analogous to natural Mg minerals containing these transition metal impurities. In this work, we report the use of synthesized mesoporous MgO nanoparticles with Cu, Fe, Zn dopants for struvite precipitation from simulated wastewater with the objective of investigating the resulting changes in reaction kinetics and product characterization.

Materials and methods

Synthesis of MgO nanoparticles (MgO NPs)

MgO NPs were prepared by a modified method previously reported.[35] An 8.7 mM $Mg(NO_3)_2$ solution was prepared by adding $Mg(NO_3)_2{\cdot}6H_2O$ (MilliporeSigma, 99%) to methanol and heating until reflux temperature was achieved. A 17.4 mM NaOH solution was prepared in methanol and added dropwise to the $Mg(NO_3)_2$ solution. After thirty minutes of reaction at reflux temperature, the precipitate was collected by centrifugation, washed three times using a 1 : 1 ratio of ethanol/water solution, and dried at 80 °C overnight. The dry solid was then calcined at 450 °C for 2 hours (2 °C min^{-1} ramp rate) in static air. Then, 0.5 g of the prepared MgO NPs was mixed in 40 ml deionized water and stirred for 12 hours. After stirring, the gel was separated and dried at 80 °C. The sample was then calcined as described earlier to obtain the final MgO NPs. Cu–MgO, Fe–MgO, and Zn–MgO samples were prepared *via* the same method by adding the appropriate metal nitrate with the $Mg(NO_3)_2{\cdot}6H_2O$. The metal nitrates used for the synthesis were copper(II) nitrate trihydrate (MilliporeSigma, 99%), iron(III) nitrate nonahydrate (Acros, 98% ACS Reagent), and zinc(II) nitrate hexahydrate (MilliporeSigma, 99%).

Struvite synthesis

Simulated NH_4^+- and PO_4^{3-}-containing wastewater samples were prepared by adding 600 ppm of monoammonium

 This journal is © The Royal Society of Chemistry 2020

Published on 28 August 2020. Downloaded by Indian Institute of Technology Kanpur on 11/11/2020 10:27:41 PM.

phosphate, $NH_4H_2PO_4$ (MAP, 99.9%, Fisher Scientific) to 18.2 MΩ cm^{-1} deionized water (Millipore, USA). The 600 ppm MAP solution represents PO_4^{3-} and NH_4^+ values found in municipal, animal and industrial wastewater[7] while maintaining the above 1 : 1 molar ratio needed for struvite formation. MgO NPs or microcrystalline MgO was added to 500 mL of the simulated wastewater and stirred for up to 120 minutes. Aliquots of 1 mL were sampled periodically, filtered through a 0.22 μm polyethersulfone filter, and analyzed using ion chromatography (IC). The MgO concentrations used for struvite synthesis were 100, 300 and 1000 ppm, which correspond to molar $[Mg^{2+}]:[NH_4^+]:[PO_4^{3-}]$ ratios of 0.48 : 1 : 1, 1.44 : 1 : 1, and 4.8 : 1 : 1. $[Mg^{2+}]:[NH_4^+]:[PO_4^{3-}]$ ratios of 0.5–1.5 : 1 : 1 have previously been tested and it was concluded that lower ratios lead to a lesser N and P adsorption/reaction.[10,36–39] Therefore, a slight excess of Mg^{2+} was preferred in previous studies to circumvent this issue and ensure efficient removal of N and P from the solution.[10,39] The microcrystalline MgO (MilliporeSigma, 99.9%) was used without further treatment.

MgO nanoparticle and struvite product characterization

The crystalline nature of all reactants and products was confirmed using powder X-ray diffraction (pXRD, Empyrean, PANalytical B.V.). The applied current was 40 mA and the applied voltage was 45 kV. The X-ray mirror that was used was a graded, flat Bragg–Brentano HD mirror, with the step size set to 0.0131 degrees. Nitrogen physisorption was used to measure surface area using a Micromeritics ASAP2020 surface area and porosimetry system. High-angle annular dark-field scanning transmission electron microscopy and energy-dispersive X-ray spectroscopy (HAADF-STEM EDS) and high-resolution transmission electron microscopy (HR-TEM) were used to confirm the bulk dopant distribution. HR-TEM imaging was performed using a JEOL2100F instrument operating at 200 kV. HAADF-STEM EDS measurements were performed using a scanning transmission electron microscope (STEM) (FEI Talos 200x) equipped with a four-quadrant 0.9 sr spectrometer for elemental and compositional mapping. A Perkin-Elmer AAnalyst200 atomic absorption spectrometer (AAS) was utilized with an air-acetylene flame to measure transition metal concentrations in aqueous solutions. X-ray photoelectron spectroscopy (XPS) analysis was carried out with a ULVAC-PHI VersaProbe III instrument using a monochromatized Al Kα X-ray source (1486.6 eV). The pass energy of the analyzer was 55.5 eV, the acquisition area had a diameter of 100 μm, and the scan step size was 0.1 eV. Binding energies were corrected for charging by referencing to the C 1s peak at 285.0 eV. Atomic concentrations were calculated from the areas under individual high-resolution XPS spectra using manufacturer-provided sensitivity factors. A Metrohm Eco 925 ion chromatography system (Herisau, Switzerland) was used to measure all aqueous ion concentrations. The separation columns used were a Metrosep A Supp 4/5 Guard column (5 × 4 mm), a Metrosep A Supp 5 (4 × 150 mm) for anion analysis and a Metrosep C 4 Guard column (5 × 4 mm) and a Metrosep C 4 (4 × 150 mm) for cation analysis. A solution of 1.75 mM HNO_3 and 0.7 mM dipicolinic acid was used as an eluent for Metrosep C 4 while a solution of 3.2 mM Na_2CO_3 and 1.0 mM $NaHCO_3$ was used for Metrosep A Supp 5 with a 0.2 M H_2SO_4 and 0.1 M $H_2C_2O_4$ suppression solution. All samples were measured at room temperature. MagIC Net 3.2 software was used to control the instrument and process the chromatograms.

X-ray absorption near-edge spectroscopy (XANES) and extended X-ray absorption fine structure (EXAFS) measurements were performed at the advanced X-ray absorption spectroscopy beamline P64 (PETRA III ring, DESY, Hamburg). Samples were mixed with microcrystalline cellulose and pressed into powder pellets. Spectra were measured at room temperature in continuous acquisition mode when the undulator and the monochromator movements were synchronized on the fly. Three ionization chambers were filled with pure nitrogen to reduce sensitivity to higher harmonics of the undulator. For each set of samples, the corresponding metal foil (Fe, Cu, Zn) was used as a standard between the second and the third ionization chambers. The monochromatic beam flux on the sample was *ca.* 5×10^{12} photons per s. The time for each spectrum was set to 5 minutes, and an average of 3–4 scans was used for the analysis. Experimental EXAFS spectra were fitted using IFEFFIT and LARCH packages.[40,41] In the fitting procedure, *ab initio* photoelectron backscattering amplitudes and phases were calculated self-consistently using FEFF8.5 code.[42] EXAFS functions were k^2- and k^3-weighted and fitted in a 1.0–3.0 Å interval of *R*-space. The range of photoelectron wave vectors used in the fit was 3.0–15.0 $Å^{-1}$. The amplitude reduction factor S_0^2 was obtained from the fit of the first shell of the corresponding standard (0.73 for Fe, 0.87 for Cu, 0.85 for Zn). Coordination numbers were fixed, different models with different coordination numbers were tested, and the best model and fit were taken. Debye–Waller factors σ^2, distances *R*, and the total energy shift ΔE_0 were varied during the fit.

PO_4^{3-} adsorption kinetics and diffusion studies

A pseudo-second-order[43] kinetic model was used to analyze the obtained PO_4^{3-} adsorption data. The linear form of the pseudo-second-order model can be expressed as (1):

$$t/q_t = 1/k_2 q_e^2 + t/q_e \quad (1)$$

where q_t (mg g^{-1}) and q_e (mg g^{-1}) are the amounts of PO_4^{3-} adsorbed at time *t* (min) and at equilibrium, respectively. k_2 (g mg^{-1} min^{-1}) is the rate constant of the pseudo-second-order kinetic model. The error bars are based on three independent measurements for each data point. To assess intraparticle diffusion effects, the Weber and Morris model was used[44] and expressed as (2)

Published on 28 August 2020. Downloaded by Indian Institute of Technology Kanpur on 11/11/2020 10:27:41 PM.

$$q_t = k_p t^{0.5} + C \quad (2)$$

where k_p (mg g^{-1} min$^{-0.5}$) is the intraparticle diffusion coefficient and C is a fitting constant.

Results and discussion

MgO NP bulk characterization

pXRD of MgO NPs. The synthesized undoped and doped MgO nanoparticles were analyzed using pXRD to confirm the MgO crystal structure. Fig. 1(a) shows the pXRD results for all precursor MgO nanoparticles. In all nanoparticles, the MgO pattern was in agreement with the reference pattern of MgO.[45] Powder XRD patterns for the doped MgO NPs showed no new peaks as dopants were introduced at 5% by weight (AAS confirmed dopant concentrations to be as follows: Cu – 4.5%, Fe – 3.8%, Zn – 4.5%). This suggests that either all dopants exist as a solid solution in the MgO cubic crystal structure by replacing Mg^{2+}, or the nanoparticles formed are under the detection limit of XRD.[46] Upon close examination of the peak of highest intensity which corresponds to the (2 0 0) plane of the MgO structure shown in Fig. 1(b), it is observed that the 2θ positions exhibit slight shifts as Cu and Zn are introduced compared to the undoped MgO. These shifts suggest that the Cu and Zn have been successfully added to the parent MgO structure and exist in solid solution rather than forming distinct nanoparticles. The Fe–MgO (2 0 0) peak did not show a significant shift from the MgO pattern. Therefore, Fe must exist in an oxide nanoparticle form (<3 nm size crystals) rather than a solid solution.

Nitrogen physisorption. Nitrogen physisorption and application of the Brunauer–Emmett–Teller equation were utilized to measure surface area. Fig. 1(c)–(f) show the BET isotherms.

The introduction of dopants did not significantly alter the BET surface area of the nanoparticles. Examination of the isotherms leads to the conclusion that all particles exhibit mesoporosity. Type IV isotherms are observed with the H3 hysteresis loop for all four NPs.[47] The pore size distributions are shown in Fig. S1.†

HAADF-STEM/EDS and HR-TEM of MgO NPs. HAADF-STEM/EDS was utilized to confirm dopant distribution and to analyze elemental composition. Fig. 2 shows the images for each precursor along with fast Fourier transforms (FFTs) of HR-TEM. The STEM/EDS shows in Fig. 2(f) and (h) that Cu and Zn are dispersed and there are no distinct nanoparticles of dopant oxides forming. The ring pattern seen by FFT of the HR-TEM images bears a similarity to other MgO nanostructures documented in the literature.[48–50] The FFT patterns shown in Fig. 2(i)–(l) insets display no new rings or distortions for any of the dopants, confirming that doping does not form large crystals of new oxide phases, but rather confirms that the dopant is introduced into the same crystal structure at MgO by replacing Mg. The STEM imaging shows

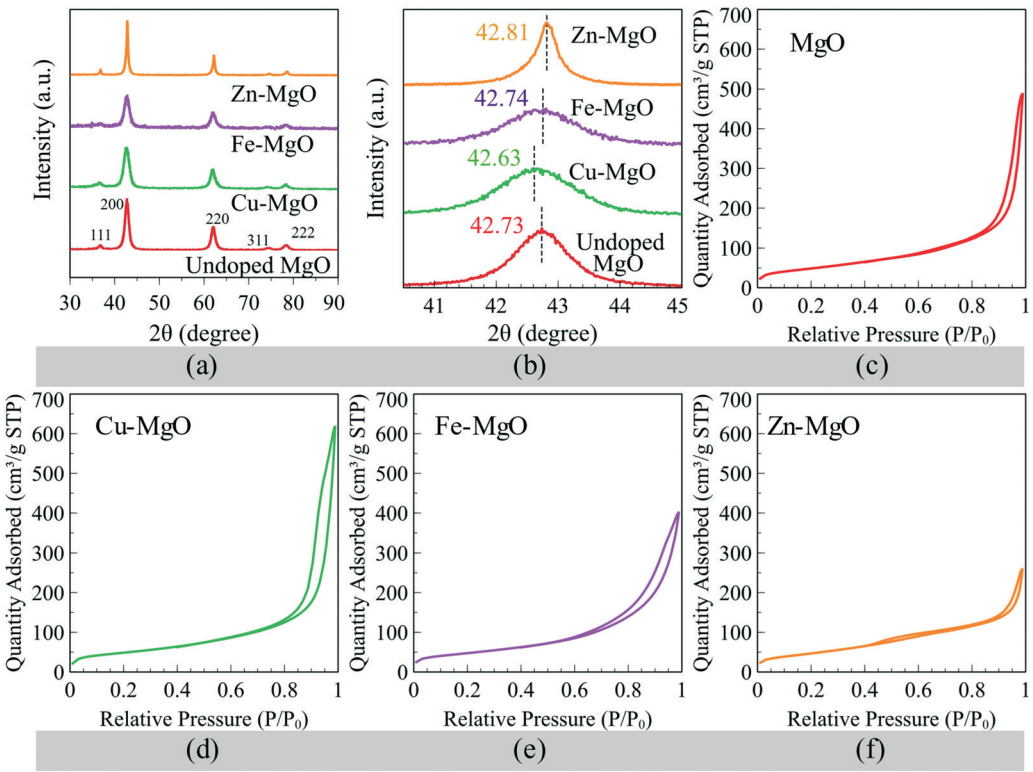

Fig. 1 (a) pXRD patterns for MgO NPs. (b) Zoomed-in pXRD peak corresponding to MgO (2 0 0) in all MgO NPs. BET isotherms for MgO NPs (c), undoped MgO (d), Cu–MgO (e), Fe–MgO and (f) Zn–MgO.

 This journal is © The Royal Society of Chemistry 2020

Published on 28 August 2020. Downloaded by Indian Institute of Technology Kanpur on 11/11/2020 10:27:41 PM.

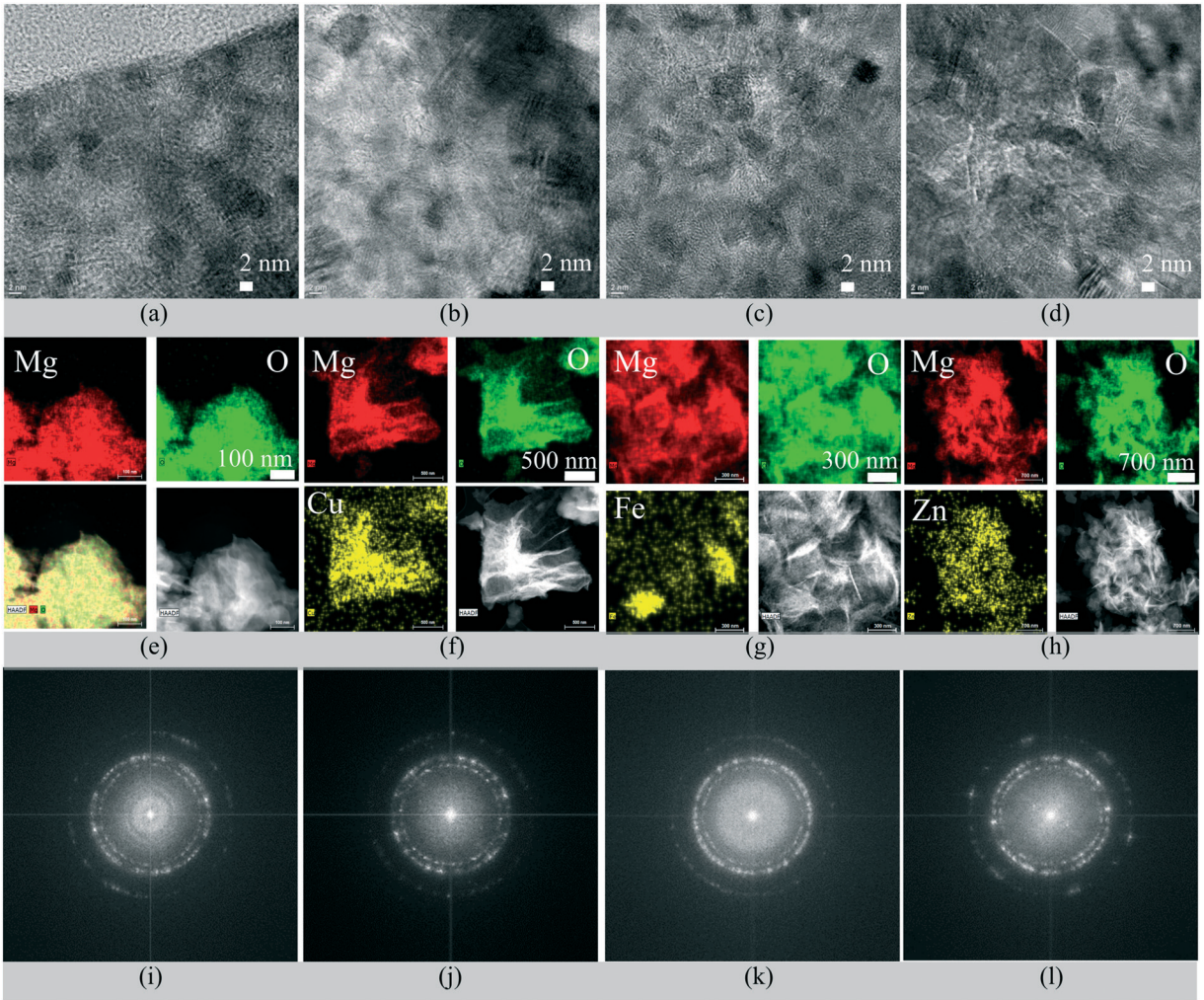

Fig. 2 HAADF-STEM EDS and HR-TEM of MgO NPs. (a)–(d) HR-TEM of MgO NPs. (e)–(h) HAADF-STEM EDS maps of MgO NPs. (i)–(l) Fast Fourier transform of the HR-TEM images of MgO NPs.

that the nanoparticles do not have a monodisperse distinct morphology but rather exist in rod-like disordered shapes. The EDS image of Fe–MgO shows that some Fe is dispersed, but also displays agglomeration pointing toward sub-3 nm oxide nanoparticle formation. Given the lack of peak shift in XRD, it can be concluded that while some small amount of Fe may form a solid solution, the majority of the Fe exists in oxide form as small crystals.

MgO NP surface region characterization

XPS of MgO NPs. XPS was utilized to study the chemical state of dopant metals in the surface region of the doped MgO NPs. The resulting Zn $2p_{3/2}$, Cu 2p, and Fe 2p spectra are shown in Fig. 3(a)–(c). The Zn $2p_{3/2}$ peak was measured at 1022.0 eV, consistent with the values of low Zn/Mg = 0.01 ratio in co-precipitated Zn/MgO and pure ZnO.[51,52] The Cu 2p core level spectrum exhibits two major peaks centered at binding energies of 934.4 and 954.0 eV, attributed to Cu $2p_{3/2}$ and Cu $2p_{1/2}$ doublets characteristic of copper(II) oxide.[53] This argument is also supported by clear shake-up peaks present at around 942.8 and 962.5 eV. Cu $2p_{3/2}$ has been reported previously at 933.7 eV for a Cu/Mg = 0.01 system prepared *via* similar chemistry and is consistent with CuO in MgO.[53] Two peaks were observed in the Fe 2p region with the apparent peaks at 712.0 and 726.2 eV due to Fe_2O_3. However, previous reports have also documented FeOOH at 711.9 eV and the possibility of the presence of a small quantity of this species cannot be ruled out.[54] A previous study has reported the presence of a peak at higher than 725 eV which shows that the presence of FeOOH is a possibility but all Fe exists in the +3 oxidation state.[55]

Atomic surface region composition, as inferred from XPS measurements, is shown in Table 2 in the form of the ratio between the corresponding metal and magnesium concentration. Approximately 5% of the surface region is composed of the corresponding metal atoms. This agrees with the bulk composition of the dopants determined using AAS measurements.

Published on 28 August 2020. Downloaded by Indian Institute of Technology Kanpur on 11/11/2020 10:27:41 PM.

MgO NP bulk electronic and molecular structure characterization

K-edge XAS of transition metal-doped MgO NPs. Ambient K-edge XANES analysis was performed to elucidate the geometry and oxidation state of the dopant transition metal ions in the doped MgO and struvite. The Cu–MgO XANES spectrum is plotted with the reference spectra in Fig. 4(a). The Cu–MgO shows a minor feature at 8977 eV which is assigned to the 1s → 3d transition (also present in $CuSO_{4(aq)}$).[56,57] The white line position is 8996 eV (consistent with CuO and $CuSO_{4(aq)}$), indicating that majority of the Cu is in the +2 oxidation state.[58,59] The lack of a pre-edge indicates that the geometry is not that of Cu_2O (which displays the pre-edge), but is consistent with CuO and $CuSO_{4(aq)}$ in elongated octahedral geometry (Jahn–Teller distortion). CuO exhibits a clear shoulder at 8986 eV, while Cu–MgO has a weak shoulder at 8987 eV. This shoulder is assigned to 1s → 4p transition.[60] The Fe–MgO XANES spectrum is plotted with the reference spectra in Fig. 4(b). The Fe–MgO minor pre-edge occurs at 7114 eV while the white line aligns at 7133 eV, both in agreement with Fe_2O_3 as well as previous reports.[61–63] Previous work done on Fe-doped MgO has shown that Fe^{3+} can exist in a Fe_2MgO_4 spinel structure, inverse spinel, and as a solid solution within the MgO structure.[58] Given the lack of peak shift in pXRD, it is more likely that nanoclusters are the prevalent structure containing the majority of the Fe. Therefore, it can be concluded that Fe is in the Fe^{3+} state octahedrally coordinated with possible Fe_2MgO_4 spinel nanoclusters or Fe_2O_3 nanoclusters. The XANES spectra for ZnO and Zn–MgO are plotted in Fig. 4(c). Analysis of Zn–MgO shows that Zn–MgO lacks a 9662 eV peak that would evidence any reduced Zn in the sample, thus confirming that all of the Zn is fully oxidized as shown in previous reports (indicating no empty d states).[57,64] The white line peak at 9670 eV for Zn–MgO is assigned to 1s → 4p, while the splitting of the feature can be attributed to Zn being present in a rigid environment.[65–67] The broad feature centered around 9680 eV is attributed to multiple scattering resonance, and the decreased intensity of the scattering peak compared to the reference tetrahedral ZnO peak is indicative of octahedral sites being present due to Zn substitution into the MgO lattice.[65] Therefore, it can be concluded that the Zn local structure differs from that of the tetrahedral structure as in ZnO to some extent.

Table 1 BET surface area for undoped and doped MgO

Sample name	BET area ($m^2\ g^{-1}$)	Pore volume ($cm^3\ g^{-1}$)
MgO	177	0.481
Cu–MgO	174	0.630
Fe–MgO	171	0.523
Zn–MgO	174	0.296
Microcrystalline MgO	94	0.219

EXAFS analysis was conducted to elucidate details on metal–oxygen (Me–O) and metal–metal (Me–Me) bond length calculation *via* fitting to theoretical models. Table S2† shows the coordination numbers used as well as the bond lengths (Å) and the Debye–Waller factor σ^2 ($Å^2$) values. The *R*-space FT-EXAFS spectrum for Cu–MgO is shown in Fig. 4(e). The details for the model Cu–MgO center are shown in Fig. S2.† The Cu–Cu and Cu–Mg bond lengths are very close in size, and thus the system is assumed to be highly disordered with a Cu and Mg mixed second shell that is difficult to resolve. However, given the Cu dispersion evident from STEM and solid solution formation indicated by the XRD peak shift, the model best fitted here assumed Mg coordinated in the second sphere. As shown in Table S2,† the Cu–O (eq.) bond length is 2.03 Å and the Cu–O (ax.) bond distance is 2.31 Å. This is in agreement with previous reports.[68] The EXAFS spectrum in Fig. 4(e) for Fe–MgO shows the Fe–O bond length to be 1.95 Å and the Fe–Me bond length to be 2.98 Å. The second shell was chosen to be Fe–Mg in the simulation but is expected to be a mix of Fe–Fe and Fe–Mg given that both models result in acceptable fits. Zn–MgO EXAFS analysis was done to calculate the Zn–O and Zn–Mg bond lengths, which were found to be 2.12 Å and 3.00 Å. The Zn–Mg path fit required an $N = 12$ value, similar to some work done in a previous report.[57] The deviations of the experimental data from the theoretical EXAFS curves show that the Zn–MgO system is highly disordered. As shown by

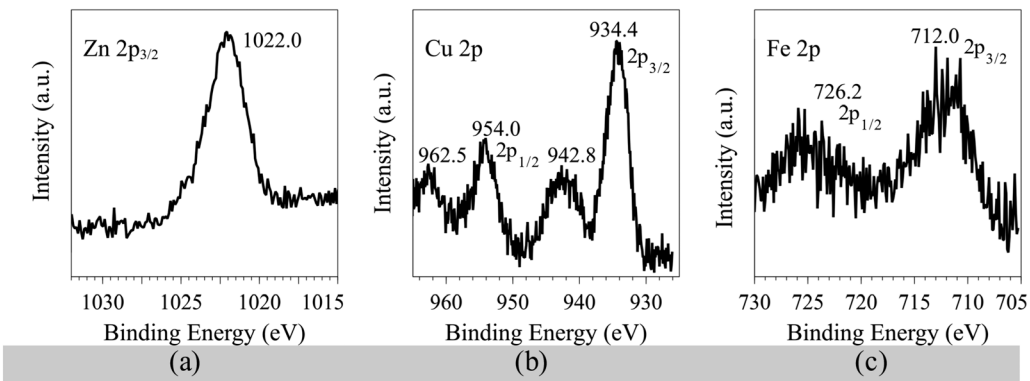

Fig. 3 High-resolution XPS spectra for MgO NPs. (a) Zn $2p_{3/2}$, (b) Cu 2p and (c) Fe 2p.

 This journal is © The Royal Society of Chemistry 2020

Published on 28 August 2020. Downloaded by Indian Institute of Technology Kanpur on 11/11/2020 10:27:41 PM.

Table 2 Surface composition of the MgO NPs as the ratio of the metal dopant 2p transition to the respective Mg 2p

Sample identifier	$Zn2p_{3/2}$/Mg2p	Cu2p/Mg2p	Fe2p/Mg2p
Cu–MgO	—	0.06	—
Fe–MgO	—	—	0.05
Zn–MgO	0.06	—	—

XANES analysis, given the suspected mixture of coordination environments for Zn, the disorder may cause the complex EXAFS spectrum.

Phosphate adsorption kinetics and ion chromatography studies

IC was utilized to measure Mg^{2+}, NH_4^+, and PO_4^{3-} ion concentrations over the 120 minute reaction time for batch experiments conducted at 25 °C. As shown in Fig. 5(a), at 100 ppm MgO loading, no adsorption of NH_4^+ was observed. This could be attributed to the low Mg^{2+} concentration not reaching the supersaturation threshold. Fig. 5(b) shows the 1000 ppm MgO loading. Here the $Mg^{2+}:NH_4^+:PO_4^{3-}$ molar ratio is 4.8 : 1 : 1, and thus supersaturation is well above the limit required for struvite crystallization. For comparison, the 1000 ppm microcrystalline MgO loading has been reported to have a transient effect on NH_4^+ adsorption[13] and this same behavior was observed here for nanostructured MgO. The 1000 ppm MgO NP loading was shown to adsorb NH_4^+ in the initial 2–10 min time but later released the NH_4^+ ions back into the solution. While the mechanistic details for the transient NH_4^+ adsorption are unclear, one hypothesis to explain this behavior could be that the increased MgO loading increases supersaturation well beyond the struvite formation limit to form $Mg_3(PO_4)_2{\cdot}22H_2O$. Fig. 5(c) shows NH_4^+ concentration as a function of time for the 300 ppm loading of MgO NPs. This was identified to be the optimal loading to produce struvite as the major product since all higher loadings produced other magnesium phosphate phases as the primary product and did not produce struvite. All PO_4^{3-} adsorption studies were conducted at the 300 ppm loading. Fig. 5(d) shows the Mg^{2+} concentration in the solution as a function of time for the 300 ppm loading. The final concentration of Mg^{2+} in the solution after the total reaction time of 120 minutes is within the 32–36 ppm range for all MgO NPs. Fig. 5(e) shows the PO_4^{3-} concentration in the solution as a function of time. The undoped MgO showed the fastest kinetics of adsorption at 25 °C with 90% PO_4^{3-} adsorbed after 10 minutes of reaction and 94% adsorption after the total reaction time of 120 minutes. Cu–MgO resulted in 90% adsorption, while both Fe–MgO and Zn–MgO led to 66% adsorption. Adding dopants exhibited lower reaction rates and equilibrium adsorbed PO_4^{3-} values compared to the undoped MgO. Finally, the undoped MgO was compared to the microcrystalline MgO as shown in Fig. 5(f).

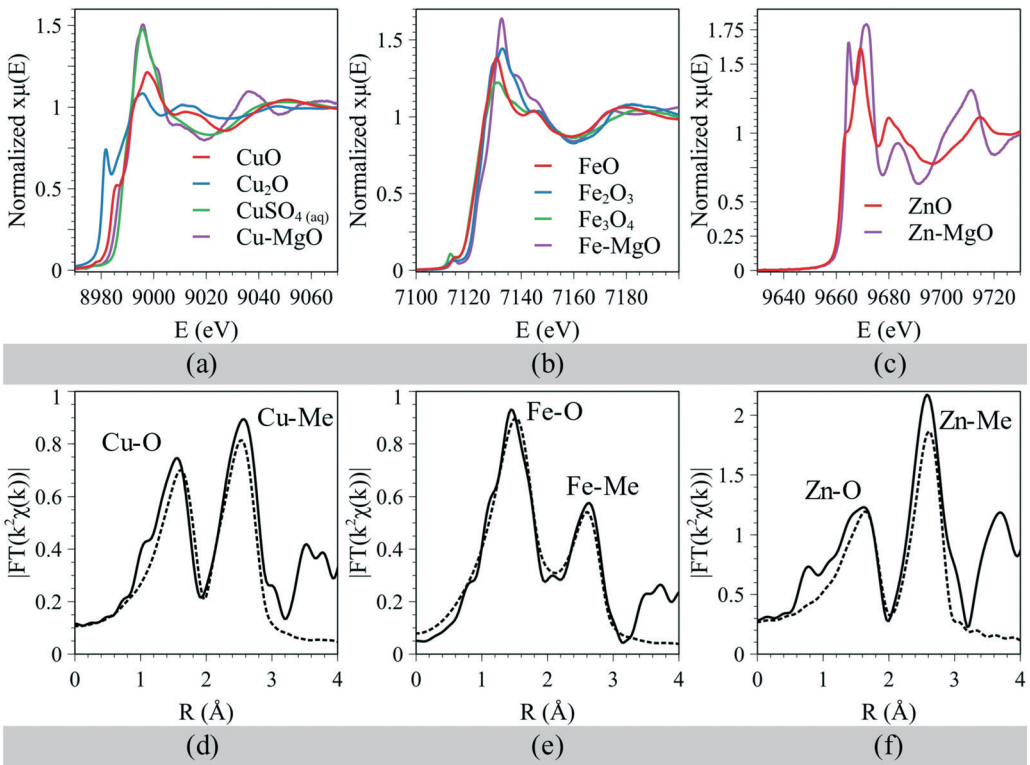

Fig. 4 Ambient K-edge XANES spectra including reference oxide standards for (a) Cu–MgO, (b) Fe–MgO and (c) Zn–MgO. Ambient K-edge FT EXAFS experimental spectra without phase shift corrections (solid line) and best-fitting model spectra (dashed line) for (d) Cu–MgO, (e) Fe–MgO and (f) Zn–MgO.

Published on 28 August 2020. Downloaded by Indian Institute of Technology Kanpur on 11/11/2020 10:27:41 PM.

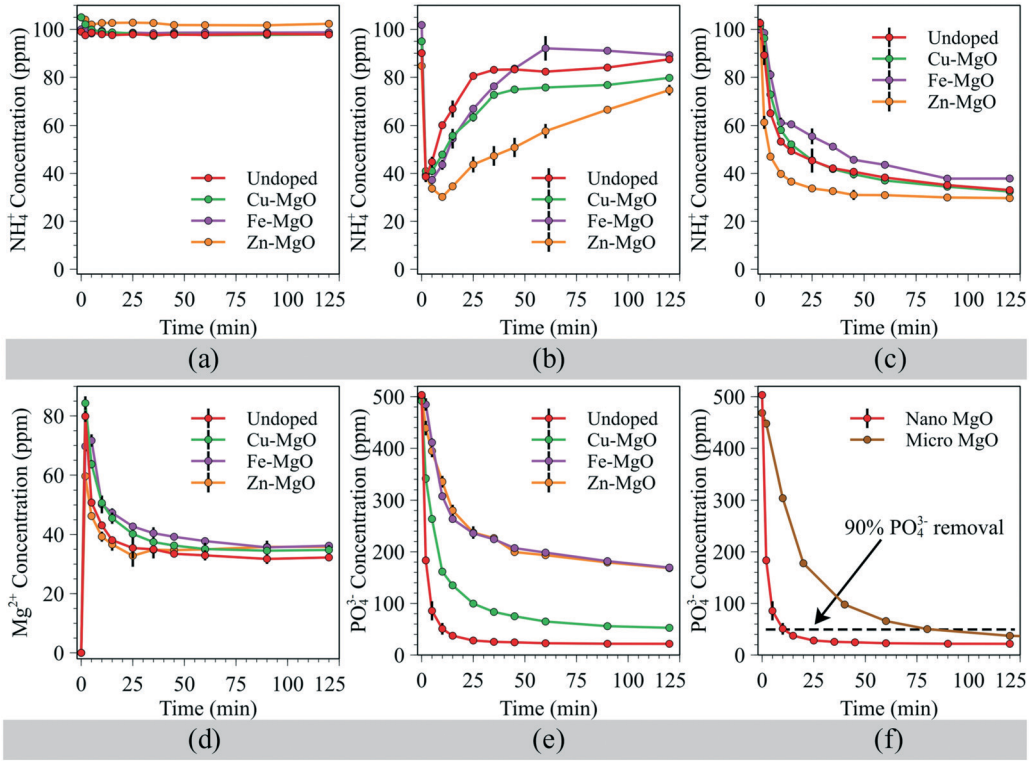

Fig. 5 Ion chromatography measurements obtained at 25 °C for undoped and doped MgO. (a) NH_4^+ concentration for 100 ppm MgO, (b) NH_4^+ concentration for 1000 ppm MgO, (c) NH_4^+ concentration for 300 ppm MgO, (d) Mg^{2+} concentration for 300 ppm MgO, (e) PO_4^{3-} concentration for 300 ppm MgO and (f) PO_4^{3-} concentrations recorded over time for undoped nano MgO and microcrystalline MgO. The dashed line shows the 90% PO_4^{3-} adsorption point for each species. Error bars represent the standard deviation for experiments performed in duplicate.

Remarkably, the undoped MgO NPs achieve 90% PO_4^{3-} adsorption after 10 minutes, while the microcrystalline MgO requires 80 minutes. The faster adsorption performance shows that the nanostructured undoped MgO can act as a more efficient PO_4^{3-} adsorbent compared to the microcrystalline MgO. The increased surface area and porosity of the nanostructured MgO (as shown in Table 1) are expected to facilitate rapid diffusion in the initial time range.

The pseudo-second-order kinetic model and the Weber and Morris model for intraparticle diffusion were used to fit the phosphate concentration profiles between 0–35 min and 0–5 min time ranges. Table S1† contains all the kinetic parameters calculated using the two models. The pseudo-second-order rate constant k_2 was used to compare the reaction kinetics for each MgO material. The rate constants calculated from the pseudo-second-order model are apparent rate constants and not intrinsic rate constants for phosphate adsorption or struvite formation. The 0–35 min time range was used since all MgO NPs are close to equilibrium after this time range. As shown in Table S1,† undoped MgO shows the highest k_2 value at 25 °C with 9.00×10^{-4} g mg^{-1} min^{-1}. Cu–MgO results in a k_2 value of 1.75×10^{-4} g mg^{-1} min^{-1} for the pseudo-second-order model. Both undoped MgO and Cu–MgO fit the pseudo-second-order model with high R^2 values ($R^2 > 0.99$). However, the Fe–MgO and Zn–MgO data did not fit the pseudo-second-order model with acceptable R^2 values. The pseudo-second-order model was chosen specifically since previous work on phosphate adsorption on MgO reported the use of the pseudo-second-order model.[13,14] The pseudo-first-order model is not applicable for this system since the theoretical work done on pseudo-first-order model derivation has shown that it provides physically meaningful information only for systems where the adsorbate concentration in the aqueous phase does not significantly change.[69,70] Therefore, only the use of the pseudo-second-order model is discussed in this report. In the temperature range of 25–45 °C, both undoped MgO and Cu–MgO fit the pseudo-second-order model with high R^2 values, while Fe–MgO and Zn–MgO showed poor fits.

The 0–5 min time range was used to assess initial reaction kinetics. As shown in Table S1,† undoped MgO data fit the pseudo-second-order model with acceptable R^2 values in this time range. However, doped MgO NPs did not fit the pseudo-second-order model in the initial 0–5 min time range as denoted by the low R^2 values. A close examination of the phosphate adsorption curves in Fig. 5(e) shows that undoped MgO displays a two-regime behavior: the fast initial adsorption from 0 to 5 minutes and the slower adsorption approaching equilibrium from 10 to 35 minutes. The doped MgO NPs did not result in this two-regime behavior. Previous studies have shown that the surface of MgO undergoes significant structural changes as well as the configurational entropic effects of the phosphate and hydrogen phosphate chain formation necessary for adsorption.[21] This complex

 This journal is © The Royal Society of Chemistry 2020

Published on 28 August 2020. Downloaded by Indian Institute of Technology Kanpur on 11/11/2020 10:27:41 PM.

surface transformation is not necessarily well described by generalized pseudo-order models. Therefore, the pseudo-order results are mainly used to describe a trend in performance rather than to elucidate absolute values.

The intraparticle diffusion effects are considered by modeling the initial PO_4^{3-} adsorption using the Weber and Morris equation.[44] The intraparticle diffusion model was used to analyze the phosphate adsorption data as shown by Fig. 6(a). Table S1† contains all intraparticle diffusion coefficient (k_p) values and the C parameter values calculated using phosphate adsorption data at 25 °C. The C parameter in the Weber and Morris equation denotes whether the surface reaction effects or diffusion effects dominate the adsorption process, with the C values indicating that diffusion is not the only dominant process and that surface adsorption is also playing a role in the rate-limiting step.[71] The diffusion effects become important in comparing the initial adsorption kinetics during the 0–5 minute time range where undoped MgO displays significantly faster kinetics, while Fe–MgO and Zn–MgO both display comparatively slower adsorption. The undoped MgO k_p was over four times the values of Fe–MgO and Zn–MgO while it exceeded 1.5 times the value of Cu–MgO. This fast diffusion may be seen as one of the reasons for the fast adsorption during the initial 5 minutes of reaction for undoped MgO. Microcrystalline MgO data fit with acceptable accuracy to show a k_p value of 177.43 mg g^{-1} $min^{-0.5}$ compared to the 618.25 mg g^{-1} $min^{-0.5}$ value of undoped MgO, which once again proves the increased efficiency advantage of nanomaterials. The increased surface area and mesoporosity allow for more favorable transport properties in the nanomaterial.

The apparent rate constant k_2 values for 25 °C, 35 °C, and 45 °C were used to construct Arrhenius plots for each MgO NP species to calculate apparent activation energies. The Arrhenius plots for the undoped and doped MgO NPs are shown in Fig. 6(b) with the R^2 values for each sample. The k_2 values calculated from undoped MgO lead to an R^2 value of 0.766 and a positive slope which is not physically meaningful. This leads to the conclusion that the apparent rate constants calculated for undoped MgO are mathematically significant, but the physical meaning lacks the mechanistic insights of surface restructuring to form the correct adsorption site for phosphate. The two-regime behavior seen in undoped MgO is not in agreement with the pseudo-second-order model, which shows that some modification to existing adsorption models is required to elucidate a physically meaningful rate constant. The Arrhenius plot for Cu–MgO shown in Fig. 6(b) fits with a high R^2 value. The apparent activation energy calculated from the slope was 23.8 kJ mol^{-1}. Given that the R^2 values for both the pseudo-second-order plots and the Arrhenius plots are high for Cu–MgO, the model-predicted k_2 value can be physically meaningful. Conversely, Fe–MgO and Zn–MgO data are poorly fitted to the pseudo-second-order model (as discussed previously) and therefore the k_2 values did not yield a good fit to the Arrhenius equation. Thus, it was not possible to calculate apparent activation energies for Fe–MgO and Zn–MgO using the pseudo-order models.

Struvite product bulk characterization

pXRD characterization of products. The products formed from the 2 hour reaction with 300 ppm loadings of MgO NPs were characterized using pXRD. All samples exhibit patterns in agreement with struvite reference PDF#15-0762 as shown in Fig. 7. No unreacted MgO peaks are present in the pXRD patterns, indicating that all MgO was fully converted. For undoped struvite and Cu-struvite, a minor peak at 11° (denoted with *) is observed. This peak is due to the presence of a small fraction of $Mg_3(PO_4)_2{\cdot}22H_2O$ (PDF#35-0186). The PO_4^{3-} adsorption in each case is slightly above a 1 : 1 ratio compared to NH_4^+ adsorption. This slight excess PO_4^{3-} removal is due to the formation of $Mg_3(PO_4)_2{\cdot}22H_2O$. The mass fraction of $Mg_3(PO_4)_2{\cdot}22H_2O$ in the case of undoped struvite production was calculated to be around 6.9% of the total product assuming that struvite and $Mg_3(PO_4)_2{\cdot}22H_2O$ are the only products. In the cases of Fe-struvite and Zn-struvite, no distinct phosphate or oxide phases are identified in the pXRD pattern, proving that the dominant crystalline product is struvite. The mass fractions of Cu, Fe, and Zn in the products were 1.0%, 1.2%, and 1.4%, respectively, as

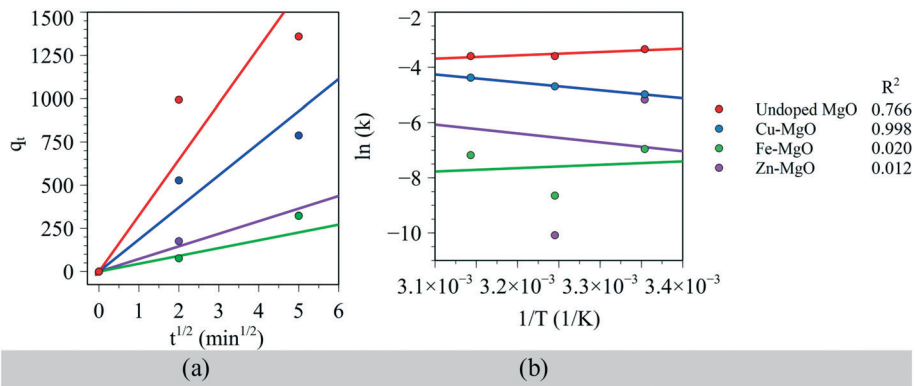

Fig. 6 (a) Intraparticle diffusion model fits for MgO NPs. (b) Arrhenius plots for MgO NPs with R^2 values.

Published on 28 August 2020. Downloaded by Indian Institute of Technology Kanpur on 11/11/2020 10:27:41 PM.

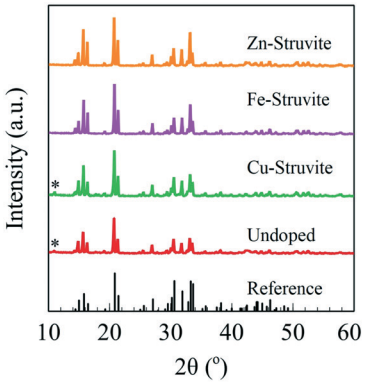

Fig. 7 pXRD patterns for products after 2 hours of reaction time (struvite reference PDF#15-0762).

measured by AAS. While Fe content in struvite is not currently regulated by European Union or the Environmental Protection Agency (EPA), the Cu and Zn contents are regulated to be 200 ppm and 600 ppm, respectively, by the EU, and 3750 ppm and 2000 ppm, respectively, by the EPA.[72,73] Given that the Cu, Fe, and Zn content for struvite formed using doped MgO exceed these limits, it is important to note that the doped struvites should be utilized after mixing with undoped struvite to meet the regulation limits and to supply the required amount of Cu, Fe, and Zn to the soil without overfertilization of micronutrients.

Struvite surface region characterization

Fig. 8 presents the XPS spectra for the reacted MgO NP products. The Zn $2p_{3/2}$ spectrum for Zn-struvite in Fig. 8(a) shows a peak at 1022.4 eV, which is consistent with literature reports for Zn^{2+} in ZnO.[74] Fig. 8(b) for Cu-struvite shows the Cu $2p_{3/2}$ peak at 932.6 eV, which has been reported in the literature as Cu_2O while also overlapping with metallic Cu.[75] The presence of metallic Cu is highly unlikely since XAS results discussed later on in the report do not indicate any presence of metallic Cu. Cu coordinated to various nitrogen ligands have been documented to have binding energies that are close to the observed 932.6 eV (ref. 76) suggesting a unique binding environment of Cu. The Fe $2p_{3/2}$ peak shown in Fig. 8(c) exhibits a broad peak centered at 711.1 eV. This suggests that in addition to the Fe_2O_3 form of Fe^{3+}, another iron atom binding configuration is likely to be present. The Fe $2p_{3/2}$ peak for $FePO_4$ was reported at 714.65 eV,[77] similar to that in $Fe_3(PO_4)_2$.[78] This shift to higher binding energies is associated with the high electronegativity of phosphate ions. The data shown in Fig. 7 for Fe $2p_{3/2}$ (and likely for Cu $2p_{3/2}$ peaks) suggest that in the surface region dopants exhibit an opposite behavior, *e.g.* they are coordinated in a manner in which the electron density is not removed from the metal nuclei. Finally, the N 1s peak is present at 401.7 eV with the corresponding P 2p peak at 133.8 eV, suggesting that the surface region contains both elements specific to struvite.

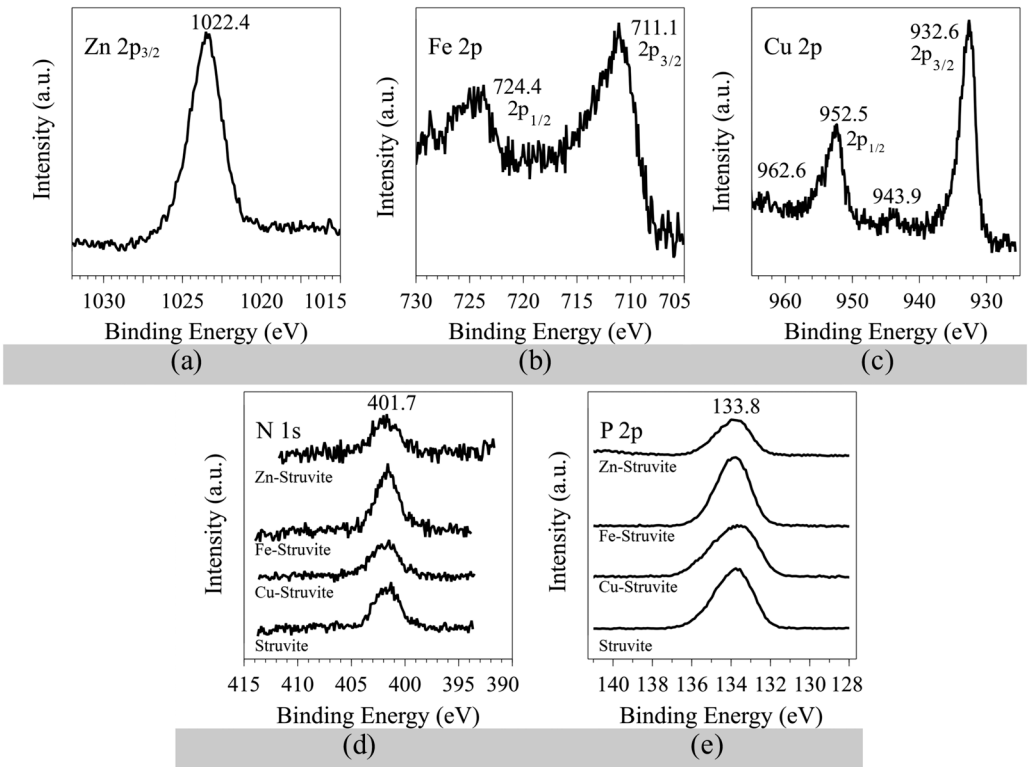

Fig. 8 XPS spectra for reacted MgO NP products. (a) Zn $2p_{3/2}$ spectrum, (b) Fe 2p spectrum, (c) Cu 2p spectrum, (d) N 1s spectra and (e) P 2p spectra.

 This journal is © The Royal Society of Chemistry 2020

Published on 28 August 2020. Downloaded by Indian Institute of Technology Kanpur on 11/11/2020 10:27:41 PM.

Table 3 Surface region composition of the reacted MgO NP products as the ratio of the area under the peak of the metal dopant 2p transition peak to the respective Mg 2p peak. An increase in the corresponding ratio from the corresponding doped MgO sample is shown in parenthesis

Sample identifier	Cu/Mg (Cu-struvite : Cu–MgO)	Fe/Mg (Fe-struvite : Fe–MgO)	Zn/Mg (Zn-struvite : Zn–MgO)	N/Mg	P/Mg
Struvite	—	—	—	0.19	0.85
Cu-struvite	0.12 (1.9)	—	—	0.23	0.95
Fe-struvite	—	0.13 (2.7)	—	0.22	0.98
Zn-struvite	—	—	0.11 (2.0)	0.08	0.32

The corresponding quantification of the dopants in the surface region is shown in Table 3. The surface region becomes enriched in dopants when compared with the corresponding MgO samples. In particular, a 1.9 to 2.7 increase in the concentration of the dopants is observed per Mg atom. An interesting observation can be made from N/Mg and P/Mg quantification in terms of the corresponding area under the peak shown in Table 3. The struvite surface region is N-deficient and in some cases, such as Zn-struvite, P-deficient even though the bulk crystallography shown in Fig. 7 corresponds to that of struvite. The P/Mg atomic ratio, on the other hand, approached that of the stoichiometric ratio of struvite of 1.

Struvite product electronic and molecular structure characterization

K-edge XAS characterization of products. The Cu-struvite Cu K-edge XANES spectrum is shown in Fig. 9(a) with reference spectra. No pre-edge is observed for Cu-struvite (similar to $CuSO_{4(aq)}$) compared to the pre-edge feature seen in the Cu_2O spectrum, indicating elongated octahedral symmetry. The Cu-struvite main edge at 8996 eV aligns within 0.5 eV of the $CuSO_{4(aq)}$ main edge. The agreement with $CuSO_{4(aq)}$ indicates that the majority of the Cu in Cu-struvite exists in elongated octahedral coordination. The white line for Cu-struvite occurs at 8996.4 eV, compared to CuO at 8997.7 eV and Cu_2O at 8995.7 eV. This indicates that a minor fraction of Cu in the Cu-struvite may be reduced as suggested by XPS results. The Fe-struvite spectrum is shown in Fig. 9(b) with the reference spectra. The Fe-struvite pre-edge feature occurs at 7114 eV with the main edge occurring at 7133 eV. This shows close alignment with the Fe_2O_3 spectrum, indicating that the majority of Fe is in octahedral coordination, similar to Fe–MgO. The Zn-struvite XANES spectrum is shown in Fig. 9(c) with the ZnO reference spectrum. Similar to Zn–MgO, Zn-struvite shows a split main feature and a scattering resonance peak. This provides

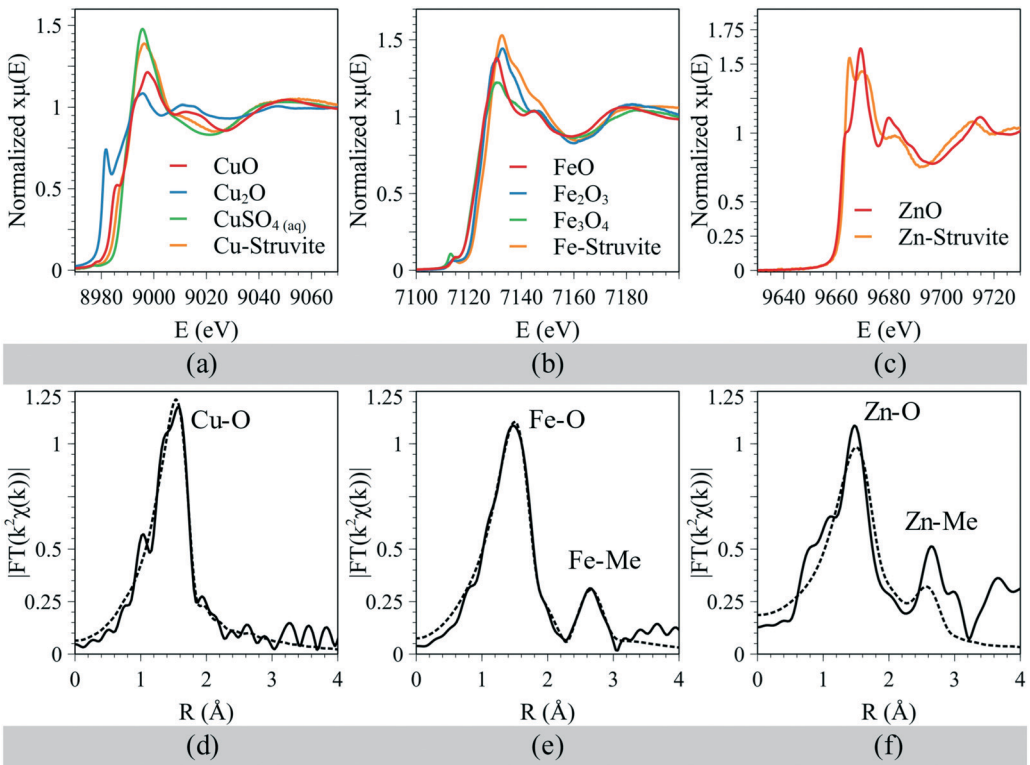

Fig. 9 K-edge XANES spectra for struvite products with reference spectra: (a) Cu-struvite, (b) Fe-struvite and (c) Zn-struvite. Ambient K-edge FT EXAFS experimental spectra without phase shift corrections (solid line) and best-fitting model spectra (dashed line) for struvite products: (d) Cu-struvite, (e) Fe-struvite and (f) Zn-struvite.

Published on 28 August 2020. Downloaded by Indian Institute of Technology Kanpur on 11/11/2020 10:27:41 PM.

evidence for the Zn local structure in Zn-struvite differing significantly from the tetrahedral ZnO structure.

The ambient K-edge EXAFS spectrum for Cu-struvite is shown in Fig. 9(d). The absence of a second shell indicates highly isolated Cu species coordinated to oxygen. The equatorial Cu–O bond and axial Cu–O distances were calculated to be 1.96 Å and 2.3 Å, while the Cu–Me bond distance was shown to be 2.96 Å. The Cu–O bond length and Cu–Cu bond length previously reported in a similar Cu–MgO system were 1.96 Å and 3.08 Å, while a standard CuO was reported to have a Cu–O distance of 1.95 Å.[57,68] The model chosen in this study shows good agreement with these literature values. The Fe-struvite EXAFS spectrum is shown in Fig. 9(e). The EXAFS spectra show the Fe–O and Fe–Me shells, which were fitted to a model with N = 6 for the Fe–O path and N = 2 for the Fe–Me path. The Fe–O bond length was calculated to be 1.95 Å and the Fe–Me bond length was calculated to be 2.98 Å. The second shell is expected to be a mixed Fe–Mg and Fe–Fe shell given the close bond lengths to that of Mg–Mg. The Zn-struvite EXAFS spectrum indicates a disordered system, leading to higher mean-square disorder values (shown in Table S2†). The Zn–O bond distance was calculated to be 1.98 Å and the Zn–Me bond distance was calculated to be 2.95 Å. The Zn–Me bond length is shorter than that in a previous report for a Zn–MgO system.[57] The EXAFS analysis of struvites shows that the dopants incorporate in a variety of coordination modes, with Cu showing highly isolated sites but Zn leading toward a highly disordered system with mixed coordination.

Conclusions

In summary, we utilized mesoporous transition metal-doped MgO nanoparticles for nutrient recycling *via* struvite synthesis from simulated wastewater. By enhancing transport properties *via* increased surface area and porosity, the nano MgO significantly outperforms the microcrystalline MgO. The undoped MgO was shown to be the best-performing adsorbent (94% PO_4^{3-} removal) while doped MgO NPs resulted in lower k_2 and q_e values, showing that dopants have an inhibitory effect on PO_4^{3-} adsorption. Understanding the chemical properties of metal ions incorporated into the MgO precursor and the struvite product is of importance in assessing whether natural MgO (which contains metal impurities) can be utilized as a sustainable Mg source for producing struvite that can be applied to agricultural systems within safety regulations imposed on fertilizer material. This study demonstrates that critical micronutrients for plant growth can be incorporated into the slow-release fertilizer struvite during synthesis from wastewater using transition metal-doped MgO (summarized in Fig. S3†), which can act as an analog to naturally occurring insoluble Mg minerals (*e.g.* periclase) with common transition metal impurities. All three dopants used in this study were micronutrients relevant to plant growth.[79,80] Zinc, in particular, is an important micronutrient to be added to soil given the Zn deficiency in US soil.[81] Incorporating Cu, Fe, and Zn in a slow-release fertilizer allows for controlled release over a long time since plants uptake micronutrients at a much slower rate compared to macronutrients such as N and P.[82]

Author contributions

V. M. acquired and analyzed XAS data. L. Z. performed microscopy studies. J. B. acquired XPS data. M. S. conducted experimental design, XRD, and IC. M. S. and J. B. wrote the manuscript.

Conflicts of interest

The authors declare no conflicts of interest.

Acknowledgements

This material is based upon work supported by the National Science Foundation under Grant No. CHE 1710120. V. M. is grateful for financial support from the BMBF project 05K19PXA. The authors acknowledge Prof. Mark Snyder and Mr. Lohit Sharma for assistance with obtaining BET data. The authors acknowledge Dr. Martin Etter for his assistance in acquiring XAS data.

References

1 J. A. Foley, N. Ramankutty, K. A. Brauman, E. S. Cassidy, J. S. Gerber, M. Johnston, N. D. Mueller, C. O'Connell, D. K. Ray, P. C. West, C. Balzer, E. M. Bennett, S. R. Carpenter, J. Hill, C. Monfreda, S. Polasky, J. Rockström, J. Sheehan, S. Siebert, D. Tilman and D. P. M. Zaks, Solutions for a cultivated planet, *Nature*, 2011, **478**, 337.

2 J. N. Galloway, J. D. Aber, J. W. Erisman, S. P. Seitzinger, R. W. Howarth, E. B. Cowling and B. J. Cosby, The Nitrogen Cascade, *BioScience*, 2003, **53**, 341–356.

3 J. N. Galloway and E. B. Cowling, Reactive Nitrogen and The World: 200 Years of Change, *Ambio*, 2002, **31**, 64–71.

4 J. N. Galloway, A. R. Townsend, J. W. Erisman, M. Bekunda, Z. Cai, J. R. Freney, L. A. Martinelli, S. P. Seitzinger and M. A. Sutton, Transformation of the Nitrogen Cycle: Recent Trends, Questions, and Potential Solutions, *Science*, 2008, **320**, 889–892.

5 S. Cheng, L. Shao, J. Ma, X. Xia, Y. Liu, Z. Yang, C. Yang and S. Li, Simultaneous removal of phosphates and dyes by Al-doped iron oxide decorated MgAl layered double hydroxide nanoflakes, *Environ. Sci.: Nano*, 2019, **6**, 2615–2625.

6 J. J. Beaulieu, T. DelSontro and J. A. Downing, Eutrophication will increase methane emissions from lakes and impoundments during the 21st century, *Nat. Commun.*, 2019, **10**, 1375.

7 T. Cai, S. Y. Park and Y. Li, Nutrient recovery from wastewater streams by microalgae: Status and prospects, *Renewable Sustainable Energy Rev.*, 2013, **19**, 360–369.

8 M. I. H. Bhuiyan, D. S. Mavinic and R. D. Beckie, A solubility and thermodynamic study of struvite, *Environ. Technol.*, 2007, **28**, 1015–1026.

 This journal is © The Royal Society of Chemistry 2020

Published on 28 August 2020. Downloaded by Indian Institute of Technology Kanpur on 11/11/2020 10:27:41 PM.

9 K. S. Le Corre, E. Valsami-Jones, P. Hobbs and S. A. Parsons, Phosphorus Recovery from Wastewater by Struvite Crystallization: A Review, *Crit. Rev. Environ. Sci. Technol.*, 2009, **39**, 433–477.
10 M. M. Rahman, M. A. M. Salleh, U. Rashid, A. Ahsan, M. M. Hossain and C. S. Ra, Production of slow release crystal fertilizer from wastewaters through struvite crystallization – A review, *Arabian J. Chem.*, 2014, **7**, 139–155.
11 I. S. A. I. Mutaz and K. M. Wagialia, Production of magnesiumfrom desalination brines, *Resour., Conserv. Recycl.*, 1990, **3**, 231–239.
12 J. Liu, M. D. Bearden, C. A. Fernandez, L. S. Fifield, S. K. Nune, R. K. Motkuri, P. K. Koech and B. P. McGrail, Techno-Economic Analysis of Magnesium Extraction from Seawater via a Catalyzed Organo-Metathetical Process, *JOM*, 2018, **70**, 431–435.
13 D. Kiani, Y. Sheng, B. Lu, D. Barauskas, K. Honer, Z. Jiang and J. Baltrusaitis, Transient Struvite Formation during Stoichiometric (1:1) NH4+ and PO43– Adsorption/Reaction on Magnesium Oxide (MgO) Particles, *ACS Sustainable Chem. Eng.*, 2018, **7**, 1545–1556.
14 P. Xia, X. Wang, X. Wang, J. Song, H. Wang and J. Zhang, Struvite crystallization combined adsorption of phosphate and ammonium from aqueous solutions by mesoporous MgO–loaded diatomite, *Colloids Surf., A*, 2016, **506**, 220–227.
15 M. Quintana, M. F. Colmenarejo, J. Barrera, G. García, E. García and A. Bustos, Use of a Byproduct of Magnesium Oxide Production To Precipitate Phosphorus and Nitrogen as Struvite from Wastewater Treatment Liquors, *J. Agric. Food Chem.*, 2004, **52**, 294–299.
16 M. Quintana, E. Sánchez, M. F. Colmenarejo, J. Barrera, G. García and R. Borja, Kinetics of phosphorus removal and struvite formation by the utilization of by-product of magnesium oxide production, *Chem. Eng. J.*, 2005, **111**, 45–52.
17 J. Li, X. Wang, J. Wang, Y. Li, S. Xia and J. Zhao, Simultaneous recovery of microalgae, ammonium and phosphate from simulated wastewater by MgO modified diatomite, *Chem. Eng. J.*, 2019, **362**, 802–811.
18 B. Lu, D. Kiani, W. Taifan, D. Barauskas, K. Honer, L. Zhang and J. Baltrusaitis, Spatially Resolved Product Speciation during Struvite Synthesis from Magnesite (MgCO3) Particles in Ammonium (NH4+) and Phosphate (PO43−) Aqueous Solutions, *J. Phys. Chem. C*, 2019, **123**(14), 8908–8922.
19 E. Kirinovic, A. R. Leichtfuss, C. Navizaga, H. Zhang, J. D. S. Christus and J. Baltrusaitis, Spectroscopic and microscopic identification of the reaction products and intermediates during the struvite (MgNH4PO4·6H2O) formation from magnesium oxide (MgO) and magnesium carbonate (MgCO3) microparticles, *ACS Sustainable Chem. Eng.*, 2017, **5**, 1567–1577.
20 J. Hövelmann and C. V. Putnis, In Situ nanoscale imaging of struvite formation during the dissolution of natural brucite: Implications for phosphorus recovery from wastewaters, *Environ. Sci. Technol.*, 2016, **50**, 13032–13041.
21 D. Kiani, M. Silva, Y. Sheng and J. Baltrusaitis, Experimental Insights into the Genesis and Growth of Struvite Particles on Low-Solubility Dolomite Mineral Surfaces, *J. Phys. Chem. C*, 2019, **123**(41), 25135–25145.
22 J. Pesonen, P. Myllymäki, S. Tuomikoski, G. Vervecken, T. Hu, H. Prokkola, P. Tynjälä, U. Lassi, J. Pesonen, P. Myllymäki, S. Tuomikoski, G. Vervecken, T. Hu, H. Prokkola, P. Tynjälä and U. Lassi, Use of Calcined Dolomite as Chemical Precipitant in the Simultaneous Removal of Ammonium and Phosphate from Synthetic Wastewater and from Agricultural Sludge, *ChemEngineering*, 2019, **3**, 40.
23 L. Chen, C. H. Zhou, H. Zhang, D. S. Tong, W. H. Yu, H. M. Yang and M. Q. Chu, Capture and recycling of ammonium by dolomite-aided struvite precipitation and thermolysis, *Chemosphere*, 2017, **187**, 302–310.
24 M. A. Barakat, *Arabian J. Chem.*, 2011, **4**, 361–377.
25 C. Tang, Z. Liu, C. Peng, L. Y. Chai, K. Kuroda, M. Okido and Y. X. Song, New insights into the interaction between heavy metals and struvite: Struvite as platform for heterogeneous nucleation of heavy metal hydroxide, *Chem. Eng. J.*, 2019, **365**, 60–69.
26 A. A. Rouff, M. V. Ramlogan and A. Rabinovich, Synergistic Removal of Zinc and Copper in Greenhouse Waste Effluent by Struvite, *ACS Sustainable Chem. Eng.*, 2016, **4**, 1319–1327.
27 A. A. Rouff and K. M. Juarez, Zinc Interaction with Struvite During and After Mineral Formation, *Environ. Sci. Technol.*, 2014, **48**, 6342–6349.
28 M. Ronteltap, M. Maurer and W. Gujer, The behaviour of pharmaceuticals and heavy metals during struvite precipitation in urine, *Water Res.*, 2007, **41**, 1859–1868.
29 A. Uysal, Y. D. Yilmazel and G. N. Demirer, The determination of fertilizer quality of the formed struvite from effluent of a sewage sludge anaerobic digester, *J. Hazard. Mater.*, 2010, **181**, 248–254.
30 W. A. Deer, R. A. Howie and J. Zussman, *An Introduction to the Rock-Forming Minerals*, Mineralogical Society of Great Britain and Ireland, 2013.
31 P. Raschman and A. Fedoročková, Dissolution kinetics of periclase in dilute hydrochloric acid, *Chem. Eng. Sci.*, 2008, **63**, 576–586.
32 N. Z. Janković and D. L. Plata, Engineered nanomaterials in the context of global element cycles, *Environ. Sci.: Nano*, 2019, **6**, 2697–2711.
33 F. Demir, O. Laçin and B. Dönmez, Leaching kinetics of calcined magnesite in citric acid solutions, *Ind. Eng. Chem. Res.*, 2006, **45**, 1307–1311.
34 J. Baltrusaitis, C. Hatch and R. Orlando, Periodic DFT study of acidic trace atmospheric gas molecule adsorption on Ca- and Fe-doped MgO(001) surface basic sites, *J. Phys. Chem. A*, 2012, **116**, 7950–7958.
35 S. W. Bian, J. Baltrusaitis, P. Galhotra and V. H. Grassian, A template-free, thermal decomposition method to synthesize mesoporous MgO with a nanocrystalline framework and its application in carbon dioxide adsorption, *J. Mater. Chem.*, 2010, **20**, 8705–8710.

Published on 28 August 2020. Downloaded by Indian Institute of Technology Kanpur on 11/11/2020 10:27:41 PM.

36 P. Stolzenburg, A. Capdevielle, S. Teychené and B. Biscans, Struvite precipitation with MgO as a precursor: Application to wastewater treatment, *Chem. Eng. Sci.*, 2014, **133**, 9–15.
37 S. K. L. Ishii and T. H. Boyer, Life cycle comparison of centralized wastewater treatment and urine source separation with struvite precipitation: Focus on urine nutrient management, *Water Res.*, 2015, **79**, 88–103.
38 K. Yetilmezsoy and Z. Sapci-Zengin, Recovery of ammonium nitrogen from the effluent of UASB treating poultry manure wastewater by MAP precipitation as a slow release fertilizer, *J. Hazard. Mater.*, 2009, **166**, 260–269.
39 T. Zhang, L. Ding and H. Ren, Pretreatment of ammonium removal from landfill leachate by chemical precipitation, *J. Hazard. Mater.*, 2009, **166**, 911–915.
40 B. Ravel and M. Newville, *J. Synchrotron Radiat.*, 2005, **12**, 537–541.
41 M. Newville, EXAFS analysis using FEFF and FEFFIT, *J. Synchrotron Radiat.*, 2001, **8**, 96–100.
42 A. Ankudinov and J. Rehr, Relativistic calculations of spin-dependent x-ray-absorption spectra, *Phys. Rev. B: Condens. Matter Mater. Phys.*, 1997, **56**, R1712–R1716.
43 Y. S. Ho and G. McKay, Pseudo-second order model for sorption processes, *Process Biochem.*, 1999, **34**, 451–465.
44 W. J. Weber and J. C. Morris, Kinetics of Adsorption on Carbon from Solution, *J. Sanit. Eng. Div., Am. Soc. Civ. Eng.*, 1963, **89**, 31–60.
45 R. M. Hazen, Effects of temperature and pressure on the cell dimension and X-ray temperature factors of periclase, *Am. Mineral.*, 1976, **61**(3), 266–271.
46 M. A. Bañares and I. E. Wachs, in *Encyclopedia of Analytical Chemistry*, John Wiley & Sons, Ltd, Chichester, UK, 2010.
47 M. Thommes, K. Kaneko, A. V. Neimark, J. P. Olivier, F. Rodriguez-Reinoso, J. Rouquerol and K. S. W. Sing, Physisorption of gases, with special reference to the evaluation of surface area and pore size distribution (IUPAC Technical Report), *Pure Appl. Chem.*, 2015, **87**, 1051–1069.
48 F. Meshkani and M. Rezaei, Facile synthesis of nanocrystalline magnesium oxide with high surface area, *Powder Technol.*, 2009, **196**, 85–88.
49 Z. Zhang, X. Fu, M. Mao, Q. Yu, S. X. Mao, J. Li and Z. Zhang, In situ observation of sublimation-enhanced magnesium oxidation at elevated temperature, *Nano Res.*, 2016, **9**, 2796–2802.
50 B. Eckhardt, E. Ortel, J. Polte, D. Bernsmeier, O. Görke, P. Strasser and R. Kraehnert, Micelle-templated mesoporous films of magnesium carbonate and magnesium oxide, *Adv. Mater.*, 2012, **24**, 3115–3119.
51 F. Khairallah, A. Glisenti, A. Galenda and M. M. Natile, Mixed Magnesium and Zinc Oxide Prepared by Co-precipitation and Analyzed by XPS, *Surf. Sci. Spectra*, 2012, **19**, 13–22.
52 P. S. Wehner, P. N. Mercer and G. Apai, Interaction of H2 and CO with Rh4(CO)12 supported on ZnO, *J. Catal.*, 1983, **84**, 244–247.
53 F. Khairallah, A. Glisenti, M. M. Natile and A. Galenda, CuO/MgO Nanocomposites by Wet Impregnation: An XPS Study, *Surf. Sci. Spectra*, 2012, **19**, 23–29.
54 N. S. McIntyre and D. G. Zetaruk, X-ray Photoelectron Spectroscopic Studies of Iron Oxides, *Anal. Chem.*, 1977, **49**, 1521–1529.
55 J. Fan, Z. Zhao, Z. Ding and J. Liu, Synthesis of different crystallographic FeOOH catalysts for peroxymonosulfate activation towards organic matter degradation, *RSC Adv.*, 2018, **8**, 7269–7279.
56 C. Angelici, F. Meirer, A. M. J. Van Der Eerden, H. L. Schaink, A. Goryachev, J. P. Hofmann, E. J. M. Hensen, B. M. Weckhuysen and P. C. A. Bruijnincx, Ex Situ and Operando Studies on the Role of Copper in Cu-Promoted SiO2-MgO Catalysts for the Lebedev Ethanol-to-Butadiene Process, *ACS Catal.*, 2015, **5**, 6005–6015.
57 W. E. Taifan, Y. Li, J. P. Baltrus, L. Zhang, A. I. Frenkel and J. Baltrusaitis, Operando Structure Determination of Cu and Zn on Supported MgO/SiO2 Catalysts during Ethanol Conversion to 1,3-Butadiene, *ACS Catal.*, 2019, **9**, 269–285.
58 K. Asakura and Y. Iwasawa, A structure model as the origin of catalytic properties of metal-doped MgO systems, *Mater. Chem. Phys.*, 1988, **18**, 499–512.
59 S. Colonna, F. Arciprete, A. Balzarotti, M. Fanfoni, M. De Crescenzi and S. Mobilio, In situ X-ray absorption measurements of the Cu/MgO(0 0 1) interface, *Surf. Sci.*, 2002, **512**, L341–L345.
60 J. H. Choy, D. K. Kim, S. H. Hwang and G. Demazeau, Cu K-edge x-ray-absorption spectroscopic study on the octahedrally coordinated trivalent copper in the perovskite-related compounds La2Li0.5Cu0.5O4 and LaCuO3, *Phys. Rev. B: Condens. Matter Mater. Phys.*, 1994, **50**, 16631–16639.
61 M. Wilke, O. Hahn, A. B. Woodland and K. Rickers, The oxidation state of iron determined by Fe K-edge XANES - application to iron gall ink in historical manuscripts, *J. Anal. At. Spectrom.*, 2009, **24**, 1364–1372.
62 A. Kuzmin and J. Chaboy, EXAFS and XANES analysis of oxides at the nanoscale, *IUCrJ*, 2014, **1**, 571–589.
63 O. L. G. Alderman, M. C. Wilding, A. Tamalonis, S. Sendelbach, S. M. Heald, C. J. Benmore, C. E. Johnson, J. A. Johnson, H. Y. Hah and J. K. R. Weber, Iron K-edge X-ray absorption near-edge structure spectroscopy of aerodynamically levitated silicate melts and glasses, *Chem. Geol.*, 2017, **453**, 169–185.
64 J. N. Harvey, *Principles and Applications of Density Functional Theory in Inorganic Chemistry*, Springer, Berlin, Heidelberg, 2004, pp. 151–184.
65 L. Galoisy, L. Cormier, G. Calas and V. Briois, Environment of Ni, Co and Zn in low alkali borate glasses: Information from EXAFS and XANES spectra, *J. Non-Cryst. Solids*, 2001, **293–295**, 105–111.
66 H. C. Wang, Y. L. Wei, Y. W. Yang and J. F. Lee, *J. Electron Spectrosc. Relat. Phenom.*, 2005, **144–147**, 817–819.
67 R. A. Kelly, J. C. Andrews and J. G. DeWitt, An X-ray absorption spectroscopic investigation of the nature of the zinc complex accumulated in Datura innoxia plant tissue culture, *Microchem. J.*, 2002, **71**, 231–245.
68 M. C. Hsiao, H. P. Wang and Y. W. Yang, EXAFS and XANES studies of copper in a solidified fly ash, *Environ. Sci. Technol.*, 2001, **35**, 2532–2535.

 This journal is © The Royal Society of Chemistry 2020

Published on 28 August 2020. Downloaded by Indian Institute of Technology Kanpur on 11/11/2020 10:27:41 PM.

69 S. Azizian, Kinetic models of sorption: A theoretical analysis, *J. Colloid Interface Sci.*, 2004, **276**, 47–52.
70 R. Kh Khamizov, D. A. Sveshnikova, A. E. Kucherova and L. A. Sinyaeva, Kinetic Models of Batch Sorption in a Limited Volume, *Russ. J. Phys. Chem. A*, 2018, **92**, 1451–1460.
71 D. A. Almasri, N. B. Saleh, M. A. Atieh, G. McKay and S. Ahzi, Adsorption of phosphate on iron oxide doped halloysite nanotubes, *Sci. Rep.*, 2019, **9**, 3232.
72 V. Halleux, EU fertilising products, 2019.
73 O. US EPA, Agriculture Nutrient Management and Fertilizer.
74 S. W. Gaarenstroom and N. Winograd, Initial and final state effects in the ESCA spectra of cadmium and silver oxides, *J. Chem. Phys.*, 1977, **67**, 3500–3506.
75 J. G. Jolley, G. G. Geesey, M. R. Hankins, R. B. Wright and P. L. Wichlacz, Auger electron and X-ray photoelectron spectroscopic study of the biocorrosion of copper by alginic acid polysaccharide, *Appl. Surf. Sci.*, 1989, **37**, 469–480.
76 T. M. Ivanova, K. I. Maslakov, A. A. Sidorov, M. A. Kiskin, R. V. Linko, S. V. Savilov, V. V. Lunin and I. L. Eremenko, XPS detection of unusual Cu(II) to Cu(I) transition on the surface of complexes with redox-active ligands, *J. Electron Spectrosc. Relat. Phenom.*, 2020, **238**, 146878.
77 Y. Wang and P. M. A. Sherwood, Iron (III) Phosphate (FePO4) by XPS, *Surf. Sci. Spectra*, 2002, **9**, 99–105.
78 Y. Wang, D. J. Asunskis and P. M. A. Sherwood, Iron (II) Phosphate (Fe3(PO4)2 by XPS, *Surf. Sci. Spectra*, 2002, **9**, 91–98.
79 K. N. Kuki, M. A. Oliva and A. C. Costa, The simulated effects of iron dust and acidity during the early stages of establishment of two coastal plant species, *Water, Air, Soil Pollut.*, 2009, **196**, 287–295.
80 I. Cakmak, Possible roles of zinc in protecting plant cells from damage by reactive oxygen species, *New Phytol.*, 2000, **146**, 185–205.
81 B. J. Alloway, *Environ. Geochem. Health*, 2009, **31**, 537–548.
82 N. K. Fageria, C. Baligar and R. B. Clark, *Adv. Agron.*, 2002, **77**, 185–268.